



A survey of the effect of cryogenic treatment and natural ageing on structural changes and second-phase precipitation in Al–Zn–Mg–Cu alloy

Gözde Altuntaş¹ · Abbas Tamer Özdemir¹ · Bülent Bostan¹

Received: 3 December 2022 / Accepted: 16 July 2023 / Published online: 8 August 2023
© Akadémiai Kiadó, Budapest, Hungary 2023

Abstract

In this work, the impacts of shallow cryogenic ($-40\text{ }^{\circ}\text{C}$) and natural ageing treatments on the precipitation of the second phases in a 7xxx alloy were investigated. Using the differential scanning calorimetry (DSC) analysis technique, transformation temperatures of the phases both in standard natural aged and naturally aged after cryogenic treatment were determined. As a result of the analyses made, the activation energies of the precipitates formed in the material were calculated with the Kissinger, Takhor and Augis-Bennett equations and their effects on diffusion were considered. With DSC analysis, nucleation characteristics of the η' phase (MgZn_2) were determined by the Avrami parameter from the Ozawa equation. Also, features and distributions of different types of precipitates were analysed by means of scanning electron microscopy (SEM), energy-dispersive X-ray spectrometry (EDS) and X-ray diffraction (XRD) techniques, respectively. Particularly, during the cryogenic and natural ageing processes, dislocation densities, strain values of the planes, texture coefficients and so subsequent after effects on the crystal structure were assessed. It was anticipated that excess dislocations generated during sub-zero treatment preferably settled on suitable planes to subside the strain energy. Finally, it was noticed that compared to natural aged samples, application of the cryogenic treatment before ageing upsurged the hardness of the material on the average by 15%. This was possibly because of the η' precipitates nucleated mainly on dislocations.

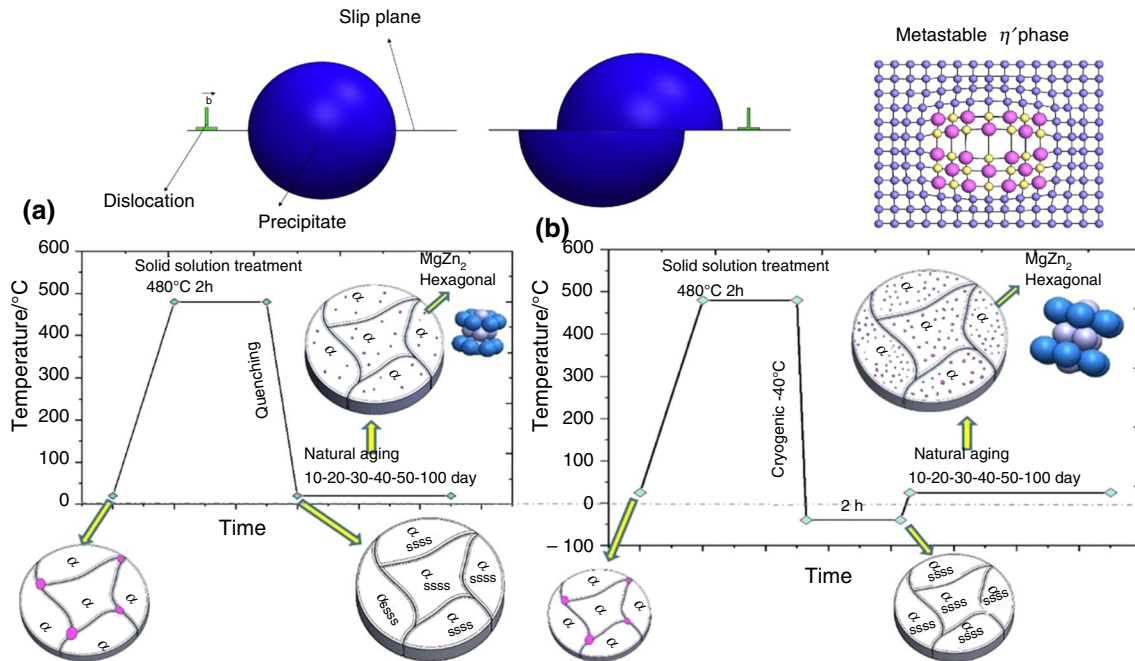
✉ Gözde Altuntaş
gozdealtuntas@gazi.edu.tr

Abbas Tamer Özdemir
tozdemir@gazi.edu.tr

Bülent Bostan
bostan@gazi.edu.tr

¹ Faculty of Technology, Department of Metallurgical and Materials Engineering, Gazi University, Ankara, Turkey

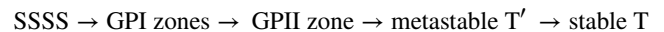
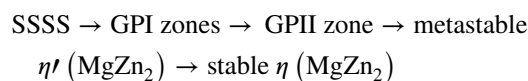
Graphical abstract



Keywords Natural ageing · Al–Zn–Mg–Cu alloy · Activation energy · Dislocation density · Cryogenic · Avrami parameter

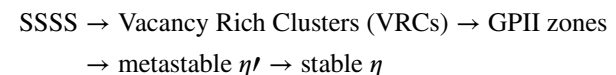
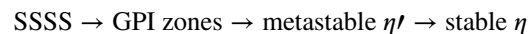
Introduction

Al–Zn–Mg–Cu (7XXX) alloys, which are used as body-building materials in the aeronautics and automotive industry, can be reached to high strength levels by various ageing heat treatment techniques [1–4]. These alloys, which normally have high ductility, naturally have good forming properties. [5]. However, their formability decreases very rapidly with the effect of ageing heat treatment and continues to change as the ageing time increases [6, 7]. After solution heat treatment and rapid quenching, a supersaturated solid solution (SSSS) is formed. During the initial stages of natural ageing, Guinier–Preston (GP) zones, which are periodically lined up in the matrix, often form homogeneously [8–10]. According to the development process, firstly, GPI as congruent-solute-rich clusters and then GPII zones consisting of gap-rich clusters are observed and are suggested as possible precursors of metastable precipitate [11–14]. In some special cases, especially GPI zones can be found in the environment even after long-term ageing. In Al–Zn–Mg–Cu alloys, η (MgZn_2), T ($\text{Al}_2\text{Mg}_3\text{Zn}_3$), S (A_2CuMg) phases are also formed as secondary phases. In general, the phase transformations in this alloy series are as shown below [15–17];



In the ageing process at high temperatures, hexagonal η phase is formed at high Zn/Mg ratios, while T ($\text{Al}_2\text{Mg}_3\text{Zn}_3$) phase can be formed at low Zn/Mg ratios. If the precipitate size exceeds a critical value, the dislocation movements become easier as the residual grains become excessively coarse and cause a decrease in strength. Thus, as η' phase causes an increase [18, 19], in contrast η phase affects the strength adversely [20, 21].

The sequence of precipitation during natural ageing has been reported in different studies as follows [22, 23];



The Zn-rich η' phase appears to occur mainly between 30 and 240 min of artificial ageing, co-existing with larger GPI regions. A significant portion of the elongated clusters are also observed during this ageing period. It has been shown that the dominant mechanism for the formation of η' at this stage is not by nucleation in larger regions, but by conversion of small GPI regions via these elongated clusters [23]. Clumps dissolved in Al–Zn–Mg alloys can cause

a strong hardening effect, but the kinetic rate of cluster is relatively low at room temperature. In recent studies, solute clusters with a wide Zn/Mg ratio have been found to form rapidly after quenching. Most of the solute clusters are rich in Zn, and increasing the number density led to a rapid strengthening [24]. It has been observed that the formation of clusters that dissolve at ~ 2 min during very early natural ageing, is followed by nucleation of the GPII region adjacent to the clusters at ~ 10 min. Furthermore, nucleation of GPII is found to be associated with GPI, but not in a single unique mechanism. Occasionally, some GPII precipitates have been observed to dissolve in the Al matrix without further transforming into η' precipitates [25]. By DSC analysis, it is observed that the formation of GP regions is governed by the migration of Zn and Mg atoms, while the precipitation of the η' metastable and η stable phase is governed by both migration and diffusion of solute atoms [26].

Even though the mechanisms are still obscure, cryogenic treatment has been introduced to many aluminium alloys in the last decade. Particularly age-hardenable aluminium alloys have considerable advantageous mechanical properties after treated at cryogenic temperatures. Several studies have shown that deep cryogenic treatment (from -150 °C to -196 °C) increases ductility [27, 28]. On the perspective of the shallow cryogenic treatment and the natural ageing, the precipitation kinetics of the main strengthening phase η has not been adequately studied yet.

This research therefore highlights the reporting of the properties of the crystallography and particularly the η phase in an Al–Zn–Mg–Cu alloy, which received shallow cryogenic and natural ageing treatments, respectively. For this purpose, various experimental techniques and mathematical models were used to analyse and evaluate the properties emerging within the microstructure. With the analyses and calculations made, natural ageing was viewed from a broad perspective.

Experimental

In the experimental study, 7075 aluminium sheet material was used. The chemical composition of the material in % by mass is given in Table 1.

The heat treatment cycle applied to the Al 7075 alloy is given in Fig. 1. Before experiments, a preliminary study was performed to determine the optimum sub-zero treatment temperature to be effective on natural ageing process. On successive tries at -40 °C, -80 °C and -100 °C for 2 h, it was found that -40 °C was the most critical level for the initiation of subsequent natural ageing. Temperatures below this degree were not sufficient to activate the GP formation in a reasonable duration of time. Thus, the typical heat treatment cycles were then planned as follows. Firstly, the solution process was carried out in an SFL (sc 1206 model) brand chamber-type horizontal high-temperature furnace

Table 1 Chemical composition of Al 7075 T651 alloy

Elements/%								
Zn	Mg	Cu	Mn	Cr	Fe	Si	Ti	Al
5.9	2.7	1.8	0.3	0.25	0.4	0.35	0.2	Balance

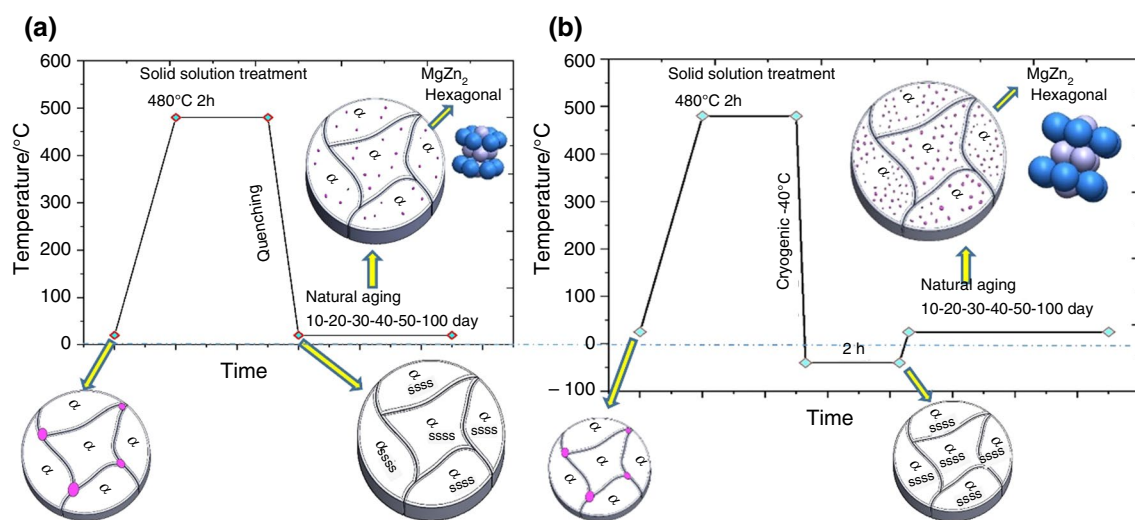


Fig. 1 Heat treatment cycles applied to Al 7075 alloy **a** natural ageing, **b** cryogenic + natural ageing

at 480 °C for 2 h. Then it was quenched and left to natural ageing for 10-20-30-40-50-100 days at room temperature. These specimens were coded as NA10, NA20, NA30, NA40, NA50, NA100. As the second step, it was taken into the solution at 480 °C for 2 h and cryogenic treatment was applied at -40 °C for 2 h in the quenching stage. Then it was left to natural ageing for 10-20-30-40-50-100 days at room temperature. These specimens were coded as CNA10, CNA20, CNA30, CNA40, CNA50, CNA100. Microhardness tests of the specimens were taken from at least 5 different points for each specimen in the Qness Hardness device according to the ASTM E384 standard, and average HV0.5 values were determined. JEOL JSM-6060LV scanning electron microscope (SEM) was used in microstructure studies. Elemental distributions were obtained with the JEOL JSM 6060LV energy-dispersive X-ray spectrometer (EDS, IXRF Sys.). X-ray diffraction (XRD) analysis was obtained using the Bruker D8 Advance instrument. Monochromatic Cu K α beam ($\lambda = 1.54056 \text{ \AA}$) was used as X-ray source, and patterns were obtained at 40 kV and 40 mA. Specimens were scanned at a scanning speed of 0.04°/min in the range of 2θ 20–90°. HITACHI DSC 7020 thermal analysis unit was used to perform differential scanning calorimetry (DSC) experiments. The tests were carried out at a temperature range of 30 °C to 480 °C in an argon atmosphere with a heating rate of 5 °C min⁻¹, 10 °C min⁻¹, 15 °C min⁻¹, 20 °C min⁻¹. It was tested with specimens of 10 mg mass enclosed in aluminium pans.

Results and discussion

The evolution of the precipitates formed by cryogenic treatment and natural ageing was investigated by DSC analysis. In Fig. 2, DSC analyses were performed at 5 °C min⁻¹, 10 °C min⁻¹, 15 °C min⁻¹, 20 °C min⁻¹. As can be seen in all specimens, the peak temperature shifted to the right as the speed increased. The transformations of the η' phases at about 180 °C and the η phases at 220 °C were detected. Similar temperature ranges were observed in most studies [29]. DSC experiments highlighted the precipitation order in the Al-Zn-Mg alloy. The shift of the peak temperature to higher temperature with increasing heating rate confirmed that the precipitation and dissolution reactions were thermally activated. As seen in Fig. 2, it was observed that the η phase transformation of the cryogenically treated specimens was at higher temperature. As it is known, the η phase is larger in size compared to the η' phase and reduces the strength [18–21, 29]. Retardation in the formation of the η phase showed that the η' phase was more dominant in the structure, where in return the strength continued to increase.

Table 2 shows the activation energies of the η' phase calculated by the Kissinger, Takhor and Augis-Bennett equations.

Kissinger equation [30];

$$\ln(\beta/T_x^2) = -(E_a/RT_x) + C \quad (1)$$

where β is heating rate, T_x is temperature of the top of the crystallization curve, R is gas constant, and E_a is the crystallization activation energy. Figure 3a, d, g, k shows NA10, CNA10, NA100 and CNA100 specimens versus $1000/T_x$ against $\ln(\beta/T_x^2)$. Using the slope of the graph of $1000/T_x$ vs. $\ln(\beta/T_x^2)$, the activation energy required for crystallization was calculated according to the Kissinger equation.

Another equation used to calculate the activation energy required for crystallization was the Takhor equation [31];

$$\ln \beta = -E_a/RT_x + C \quad (2)$$

Thus, β is heating rate, T_x is temperature of the top of the crystallization curve, R is gas constant, and E_a is the crystallization activation energy. Figure 3b, e, h, l shows $\ln(\beta)$ vs. $1000/T_x$ plot of NA10, CNA10, NA100 and CNA100 specimens. Using the slope of this graph, the activation energy required for crystallization was calculated.

Finally, the third equation used to calculate the crystallization activation energy was the Augis-Bennett equation [32];

$$\ln(\beta/T_x - T_0) = -E_a/RT_x + \ln K_0 \quad (3)$$

In this equation, β is heating rate, T_x is temperature of the top of the crystallization curve, T_0 is absolute temperature, R is gas constant, and E_a is crystallization activation energy, K_0 is the frequency factor. In Fig. 3c, f, j, m, the plot of NA10, CNA10, NA100 and CNA100 specimens vs. $1000/T_x$ is presented. Using the slope of this graph, the crystallization activation energy is calculated. The change in the activation energy calculated by the Kissinger and Takhor equations was also obtained in the Augis-Bennett equation calculations.

An up hill energy barrier (i.e., activation energy) is required for the movement of atoms during diffusion. In general, a lower activation energy indicates easier diffusion. In the present work, activation energies evaluated for the η' precipitation from Fig. 3 are listed in Table 2. It was observed that the activation energy of the CNA10 specimen increased during the 10-day ageing period. As can be understood from here, it is seen that diffusion is more difficult in the formation of the η' phase compared to the Arrhenius equation given in Eqs. 4 and 5 [33].

In a previous work, compared to classical ageing process, due to the effect of the deep cryogenic treatment (-146 °C), quench sensitivity diminished and number of imperfections minimized as the temperature decreased. In response

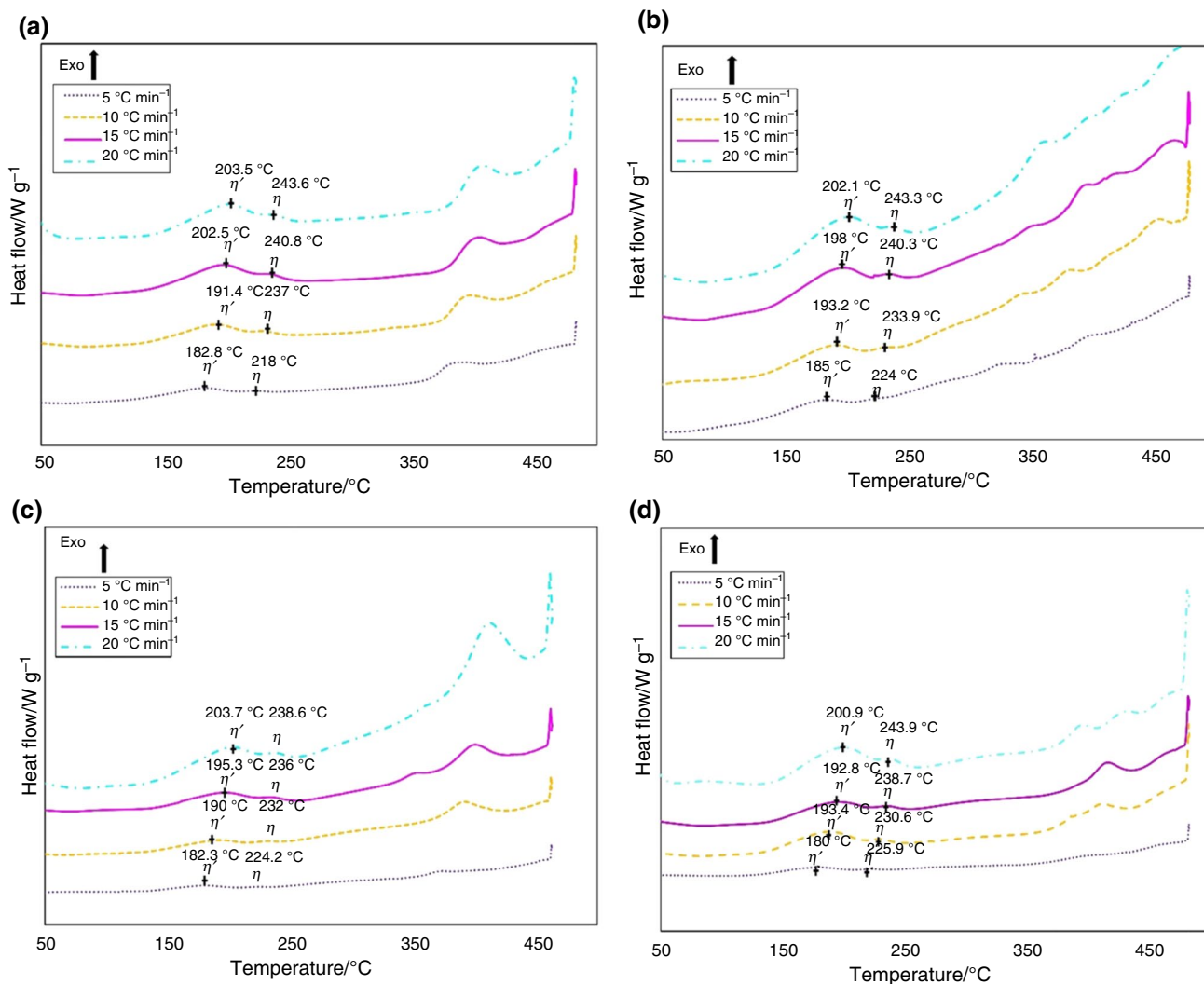


Fig. 2 DSC graphs of specimens at different speeds a NA10, b CNA10, c NA100, d CNA100

Table 2 Crystallization activation energy for the η' precipitate formed in the specimens as a result of heat treatments

Specimens	Crystallization activation energy E _a (kJ mol ⁻¹)		
	η' (MgZn ₂) precipitation		
	Kissinger	Augis-Bennett	Takhor
NA10	116	124	115
CNA10	127	135	126
NA100	105	113	104
CNA100	105	112	103

Cu-, Mg- and Zn-rich ultra-fine precipitates of GP and η' appeared successively during the current artificial ageing treatment [34]. Accordingly, difficulty in diffusion might be directly related to the vacancy concentration in the structure. After homogenization and quenching, during deep cryogenic

treatment, supersaturated aluminium developed an steady structure with less imperfections to reduce internal energy or entropy. Solute elements organized a more tiny and uniform distribution at the atomistic measure, where dislocations were less in number with specific distributions. As quench sensitivity faded away, subsequently vacancy and dislocation concentrations decreased considerably.

In the present work, as mentioned before, a pilot test was performed to determine the optimum temperature for shallow cryogenic treatment. Several specimens were treated -40 °C, -80 °C and -100 °C successively. Natural ageing could only initiated after -40 °C cryogenic treatment, where the transient gaps decreased with ageing in the first 10 days after the shallow cryogenics route. Fascinatingly, results displayed that the activation energies evaluated for both NA100 and CNA100 specimens decreased over the time towards the end of the 100-day period of

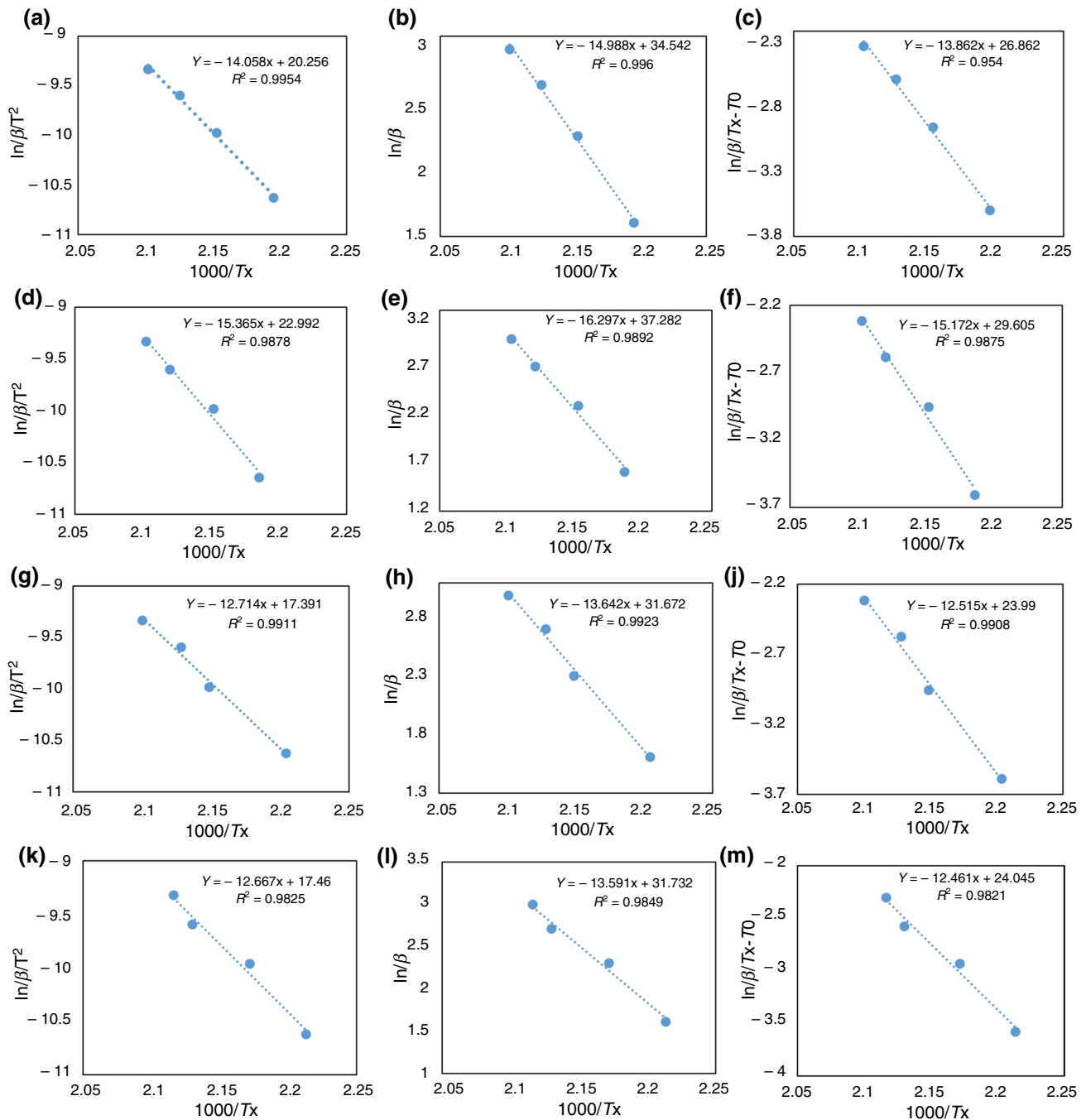


Fig. 3 Slope graphs for the activation energies of the specimens. **a, b, c** Kissinger, Takhor, Augis-Bennett slope graphs for NA10 specimen, respectively. **d, e, f** Kissinger, Takhor, Augis-Bennett slope graphs for the CNA10 specimen, respectively. **g, h, j** Kissinger, Takhor, Augis-

Bennett slope graphs for SNA100 specimen, respectively. **k, l, m** Kissinger, Takhor, Augis-Bennett slope graphs for the CNA100 specimen, respectively

the natural ageing (Table 2). Thus, as the ageing time increased, the atomic mobility of the alloying elements participating in the formation of the η' phase, became significant. This might be due to the governing room temperature conditions, where increase in time resulted in a rise

in vacancy concentration, where their number upturned to the thermodynamic level of the equilibrium concentration. Consequently, both GP and later η' precipitation encouraged in the microstructure with an ease till the consumption of the supersaturation in the aluminium matrix.

$$D = D_0 \cdot e^{-E_a/RT} \quad (4)$$

Here, D is diffusion coefficient, D_0 is diffusion constant, E_a is activation energy, R is gas constant ($8.314 \text{ J mol}^{-1} \text{ K}$), T is shown as temperature (K).

$$k = A \cdot e^{-E_a/KpT} \quad (5)$$

Here, k is reaction rate, A is exponential factor, E_a is activation energy, Kp is Boltzmann constant ($8.314 \text{ J mol}^{-1} \text{ K}$), T is shown as temperature (K). The Arrhenius equation was used to determine the reaction rate.

XRD studies

Figure 4a displays the XRD patterns of the material subjected to natural ageing at specific times, and similarly, Fig. 4b shows that of cryogenic plus naturally aged. A standard reference pattern (PDF 03-065-2869) for aluminium was used to detect crystallographic planes. It was used for MgZn_2 precipitates (PDF 01-077-1177), for $\text{Al}_7\text{Cu}_2\text{Fe}$ (PDF 03-065-1685) and for $\text{Al}_{23}\text{CuFe}_4$ (PDF 03-065-7654). With XRD analysis, it was determined that the phase volume ratios of intermetallics such as $\text{Al}_{23}\text{CuFe}_4$ and $\text{Al}_7\text{Cu}_2\text{Fe}$ increased in sub-zero treated specimens. In addition, with the increase of ageing and cryogenic treatment time, an increase in the volume ratio of the η' (MgZn_2), which is the main strengthening phase, was observed. The highest peak of the NA10 specimen, which was aged for 10 days, was observed in the (200) plane. In the NA20 specimen, the highest peak was at (111) plane. This plane showed the most intense XRD peak proposed for Al alloys [35]. In the NA30-NA40 specimens, which were aged for 30 and 40 days, the highest peak was again shown in the (200) plane. In the NA50 and NA100 specimens, the highest peak intensity was the (220) plane. The results show that increasing the natural ageing time changed the order of dense planes. In the CNA10 specimens the highest peak of the plane (200) was in competition with the (111) plane. The same trend continued in CNA20, CNA 30 and CNA40 specimens as the (200) plane was the highest, respectively. Standard natural aged and cryogenics plus natural aged specimens up to 40 days showed the highest peak in the same manner. The most intense plane of the CNA50 specimen differed from the NA50 specimen, and the highest peak was observed in the (200) plane. The CNA100 specimen, on the other hand, showed the highest peak in the suggested densest plane, namely (111). Thus, after the cryogenic process, during ageing, the most intense peak intensity returned to the recommended (111) plane at the end of 100 h. Changing the dense planes means, altering the most habit planes of the material. Thus, in this work an unsteady texturing

took place, where the change in the crystal inclination had to be limited because of the requirement of coherency at the grain boundaries. Currently to determine the degree of texture in polycrystalline materials [36], the texture coefficient of the specimens has to be calculated. In the present study, texture coefficients were calculated by the Harris analysis.

Harris analysis [37]

$$P(hkl) = \frac{I(hkl)}{I_o(hkl)} \left[\frac{1}{1/n \sum_{i=1}^n \frac{I(hikili)}{I_o(hikili)}} \right] \quad (6)$$

According to the equation, if $P(hkl) > 1$, it had orientation on the crystallographic plane (hkl). The texture coefficient values of the four crystallographic planes of natural aged specimens (111), (220), (200) and (311) were determined, and results are listed in Table 2. It was observed that the NA10, NA20, NA30 specimens textured in the (200) and (311) planes. It was clear that the orientations were in the (200) and (220) planes at the end of the natural ageing period of 40 days. After 50 days, orientation in the (220) and (311) planes was observed in the NA50 specimen. As seen in the NA100 specimen, it was clear that the orientation in the (220) plane continued as the natural ageing time increased, where the (311) plane orientation was also intensified. It was observed that CNA10-CNA20-CNA30 specimens dominantly oriented in the (311) plane. Further, CNA40 and CNA50 specimens both intensified at (200) and (311) orientations, respectively. Finally, CNA100 specimen had (220) and (311) textured planes progressively. The reason for the different orientations in the specimens is thought to be related with the surface tension of the planes. Normally atoms tend to incline towards the plane with low interfacial energy [38]. Since the interfacial energy of the (311) plane was lower in the CNA10-20-30 specimens, it was thought that the orientation proceeded only in this plane. During thermal contraction and expansion route of the cryogenic treatment, due to elastic constraints and so induced microplasticity, excess dislocations were generated and mostly arranged on low-energy high-density planes of (111) to somewhat reduce the strain energy. Then the crystal tilt is then tended to the (311) plane to control the increase in energy. The data obtained from Eq. 7 showed the lattice strain values formed by all specimens in each plane. As given in Table 3 and 4, except for the NA40 specimen, in all other natural aged specimens, lattice strains of the (220) and (311) planes were quite high. As understood from all through, the strain value of the dominant plane was high. Thus, at the end of the natural ageing period of 40 days, the planes realigned as the interfacial energy period changed.

Debye-Scherrer's formula [39]

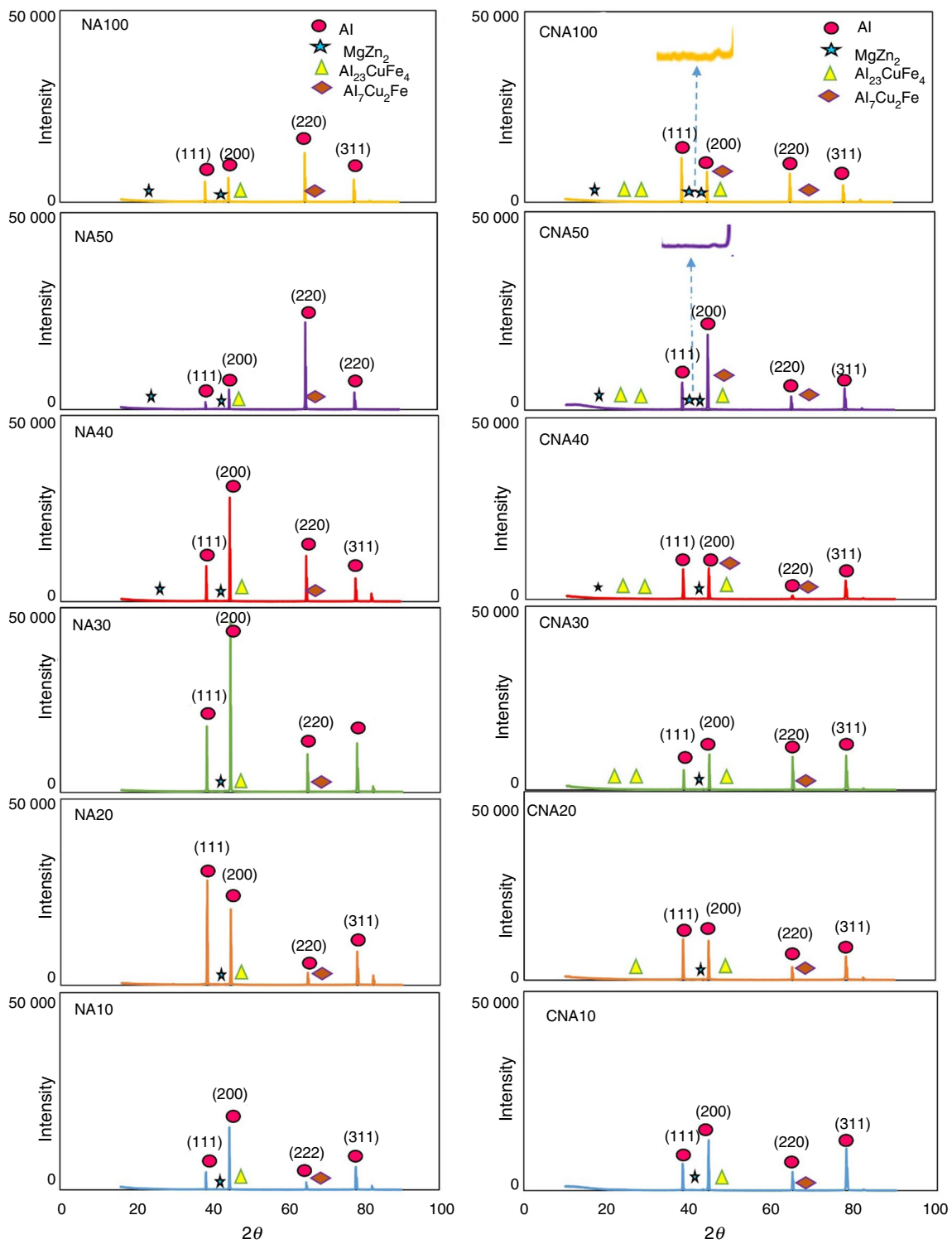


Fig. 4 XRD patterns of specimens **a** natural ageing, **b** cryogenic + natural ageing

$$\varepsilon = \beta/4 * \tan\theta \quad (7)$$

Here β = FWHM of a diffraction peak (radyan), ε = lattice strain.

By using Eqs. 8 and 9, the changes in dislocation densities were calculated according to the Williamson–Hall equation.

According to Williamson–Hall equation [40]

$$\beta * \cos \theta = k * \lambda / D + 4\epsilon \sin \theta \tag{8}$$

$$\delta = 1/Dp^2(\text{lines/m}^2) \tag{9}$$

Here,

β = FWHM of a diffraction peak (radyan).

$k = 0.94$ (for cubic structures).

$\lambda = 0.15406$ nm X-ray wavelength (Cu-K α radiation).

D = crystallite size.

ϵ = lattice strain.

The dislocation density (δ) is calculated by following formula

As clear from Figs. 5 and 6, cryogenic treatment had a profound effect in both increases in the dislocation density and the hardness of the material. However, instead of a gradual increase, dislocation density suddenly dropped down at 40 h of ageing. The reason why the hardness values were high and at first glance could be explained by a mechanism similar to that of Hall–Petch [41]. Thus, dislocation network arrangements might be effective in controlling the plastic flow, as in the case of the application of the deep cryogenic treatment. However, as mentioned before, for the present

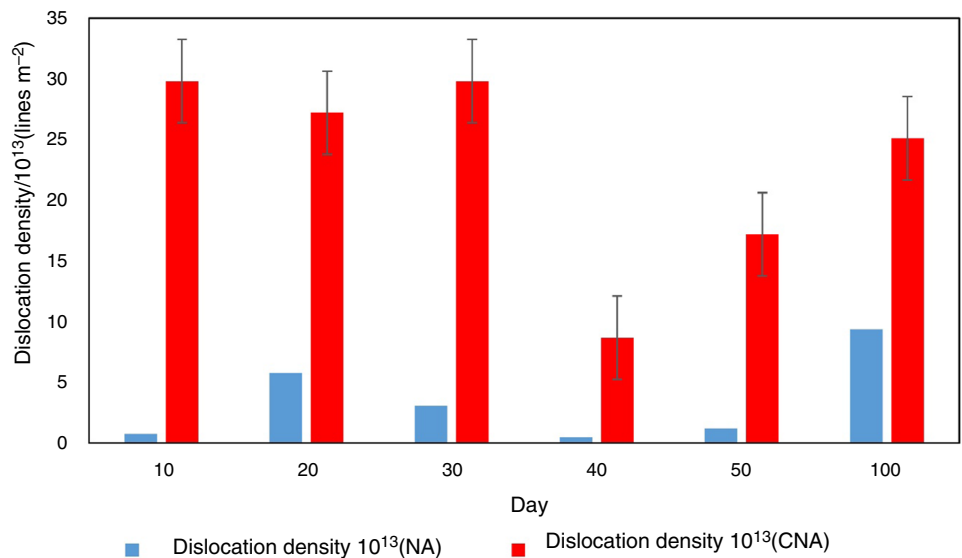
Table 3 The texture coefficient values of the specimens

Texture coefficient P (hkl)									
Specimens	111	200	220	311	Specimens	111	200	220	311
NA10	0.21	1.89	0.46	1.40	CNA10	0.27	0.91	0.85	1.95
NA20	0.92	1.38	0.44	1.24	CNA20	0.55	0.92	0.79	1.42
NA30	0.32	1.85	0.99	1.02	CNA30	0.20	0.65	0.48	1.60
NA40	0.25	1.39	1.63	0.71	CNA40	0.62	1.35	0.27	1.74
NA50	0.06	0.35	2.99	1.01	CNA50	0.32	1.08	0.67	1.91
NA100	0.21	0.55	2.20	1.02	CNA100	0.56	0.86	1.04	1.60

Table 4 Lattice strain values of crystallographic planes in specimens

Strain values of planes									
	111	200	220	311		111	200	220	311
NA10	0.00012	0.00011	0.00018	0.00050	CNA10	0.00016	0.00029	0.00032	0.00054
NA20	0.00020	0.00015	0.00024	0.00040	CNA20	0.00016	0.00015	0.00031	0.00056
NA30	0.00010	0.00010	0.00024	0.00034	CNA30	0.00016	0.00028	0.00041	0.00044
NA40	0.00013	0.00010	0.00032	0.00021	CNA40	0.00014	0.00016	0.00090	0.00062
NA50	0.00010	0.00011	0.00022	0.00041	CNA50	0.00018	0.00018	0.00031	0.00047
NA100	0.00011	0.00014	0.00018	0.00032	CNA100	0.00033	0.00031	0.00036	0.00048

Fig. 5 Dislocation densities of natural ageing (NA) and cryogenic plus natural ageing (CNA)



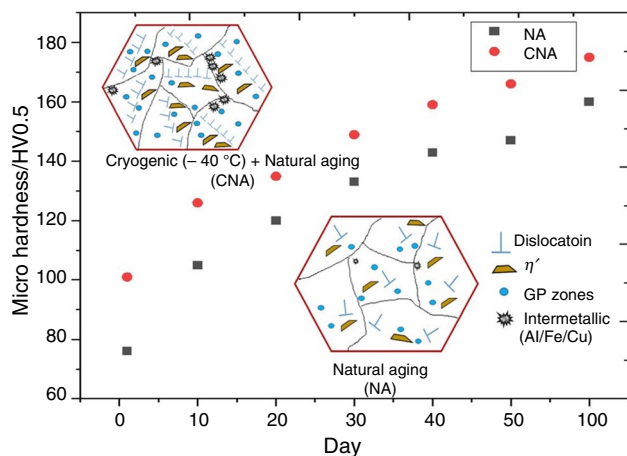


Fig. 6 Hardness values of specimens and systematic microstructure transformation

shallow cryogenics conditions, thermal contraction and expansion could introduce microplasticity-induced excess imperfections inside the crystal. Thus, there was a remarkable increase in hardness right after the cryogenic treatment. Systematic increase in strength could simply be attributed to the increased number of excess dislocations generated due to induced microplasticity after the sub-zero treatment. At the beginning of ageing up to 30 h, dislocation density was high. However, at 40-h ageing time, dislocation density dropped down considerably. On further ageing density again elevated gradually. This was possibly due to excess imperfections, mainly dislocations. At the onset of ageing, systematic increase in strength was possibly because of the creation of fine GP zones, consuming up the excess vacancies. Simply, high precipitation densities could be reached by introducing a high dislocation density into the supersaturated solid solution. In the present work, it was anticipated that the change in hardness might be a matter of stacking fault energy of the extended dislocations. Accordingly, the greatest efficiency in lowering the strain energy and therefore the activation energy for the onset of precipitate nucleation could be expected by dissociation of the dislocations into extended parts. Nucleation event could be involved on the stacking faults with a two-dimensional characteristic, rather than the one-dimensional dislocations [42]. The segregation of solute atoms towards existing stacking faults, was thought to lower the fault energy. Therefore, at this critical ageing time of 40 h, the dissociated dislocations increased in number and so dislocation density reduced considerably.

At the same time, the Avrami parameter (n) was calculated by DSC analysis according to the Ozawa [43] equation as specified in Eq. 10. In the CNA10 example, the Avrami parameter was calculated as $n = 1.73$. This result showed that there was a volumetric nucleation and two-dimensional growth of the η' phase precipitation. By calculating $n = 0.87$

in the CNA100 specimen, it was observed that this time the η' precipitates nucleation was planar and precipitates grew only in one dimension [44, 45]. Based on these facts, it was thought that the two-dimensional growth of the η' precipitates might increase the dislocation density during the first 10 days. However, at the end of 100 days, due to one-dimensional growth of the η' precipitates, dislocation density decreased remarkably.

Thus, Ozawa equation is given as follows,

$$n = \frac{d[\ln(-\ln(1-x))]}{d\ln(\beta)} \quad (10)$$

where β is the heating rate; x is the conversion rate.

In contrast, during 10, 20, 30, 40, 50 and 100 days of standard natural ageing process, hardness values were found to be continuously increasing as 105, 120, 133, 143, 147 and 160 HV0.5, respectively. On the other hand, after cryogenic treatment during the sequences of the natural ageing progression, hardness values were then measured as 126, 135, 149, 159, 166 and 175 HV0.5, respectively. These results were in fact progressively closing to that of conventional artificial ageing treatment at high temperature of 120–180 °C [5, 7, 19, 27].

During the progression of ageing, besides the GP zones, η' (MgZn_2) phase precipitates being either rod or plate-like in shape increased in number and size by impinging on the dislocations. Thus, to reduce the precipitate-matrix interfacial energy, semi-coherent and metastable η' precipitates preferentially settled on the dislocations [34] and to reduce the mis-fit or strain energy around the precipitate, dislocation loops form precipitate-matrix interfaces were possibly generated, resulting in a continuous increase in dislocation density. All these factors could cause a considerable increase in hardness [46–48].

The changes in the microstructure as a result of the heat treatments are shown in Fig. 7. Figure 7a shows the microstructure of the 100 days naturally aged NA100, and Fig. 7b shows the microstructure of the 100 days naturally aged CNA100 after the cryogenic treatment. After as clear from the figure, white coloured secondary-phase colonies at certain regions were detected in the matrix. EDS and mapping analyses were therefore performed to determine the elemental distributions of these phases (Fig. 8).

Thus, Fig. 8a displays an EDS and mapping analysis to see the elemental distributions on the microstructure of the 100-day naturally aged NA100 specimen. It was seen that in the mapping analysis, the Al–Zn–Mg–Cu elements were homogeneously distributed. Figure 8b shows the EDS and mapping analysis of the CNA100 specimen, which was naturally aged for 100 days as a result of cryogenic treatment, from 4 different regions. The white regions observed in the microstructure images were found to be Cu-rich secondary

Fig. 7 SEM images of specimens after heat treatment a NA100, b CNA100

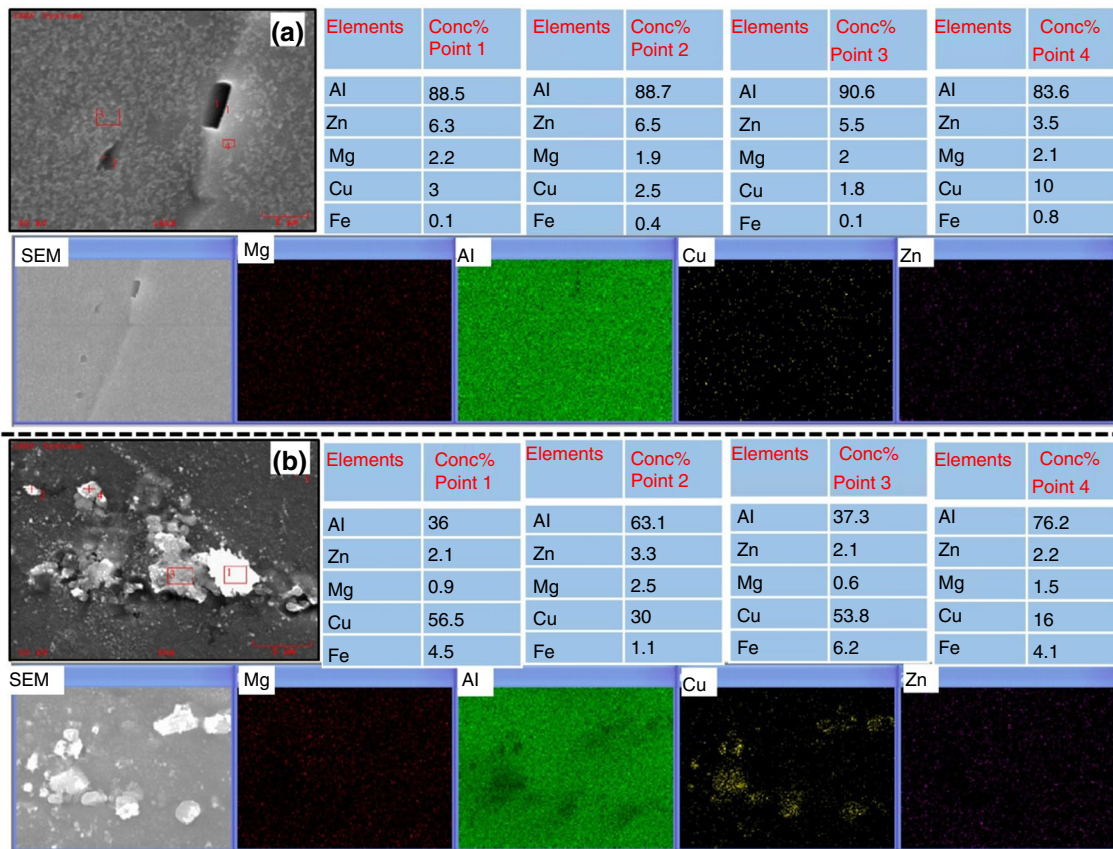
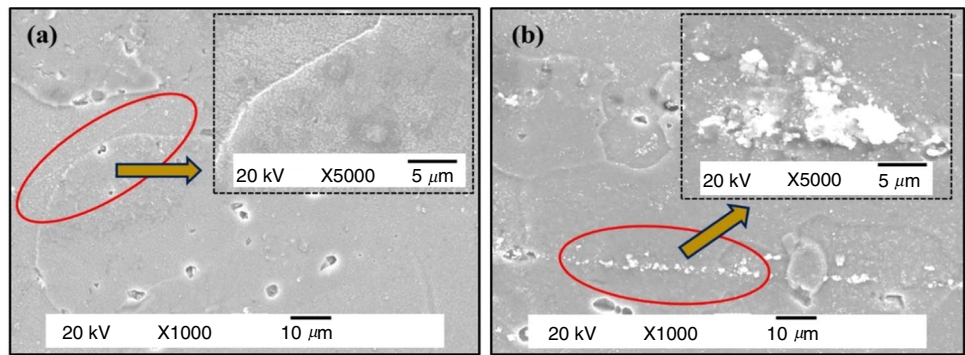


Fig. 8 EDS and mapping analysis of specimens a NA100, b CNA100

phases. The high Fe ratio in these regions indicated that cryogenic treatment increased the ratio of intermetallics such as $Al_{23}CuFe_4$ and Al_7Cu_2Fe . Secondary-phase particles such as $Al_{23}CuFe_4$ and Al_7Cu_2Fe occurred during casting or solidification processes. During homogenization of Al 7075 material, it might undergo phase transformation and their morphology could change. These precipitates had larger dimensions and a high modulus of elasticity and were not consistent with the aluminium matrix. In addition, the distribution and amount of secondary phases such as $Al_{23}CuFe_4$

and Al_7Cu_2Fe , which are formed more frequently as a result of cryogenic treatment, help to strengthen the aluminium alloy [49, 50]. In addition, the presence of intermetallics was detected by XRD analysis as seen in Fig. 4.

Accordingly, it was proposed that during ageing, heterogeneous precipitation on dislocations could lead to high precipitate densities at certain regions as to lie in strings along certain directions [42]. However, particularly after cryogenic sub-zero cooling, discrete particles were found to nucleated on the existing dislocations during ageing. They grew partially coherent

with the matrix to accommodate the strains arising from the difference between the two lattices. Possible prismatic dislocation loops were created at the expense of the growing precipitates. As ageing progresses, these loops formed the basis of new precipitation, and so long stringers of precipitation were generated.

Conclusions

In this study, natural ageing and cryogenic plus natural ageing processes were applied to Al–Zn–Mg–Cu alloy for certain periods and its effect on precipitation kinetics was investigated by DSC analysis. In addition, crystallographic analyses were studied in detail with XRD analysis and their relationship with mechanical properties was discussed and the following results were obtained.

- The transformation temperature of the η phase was found to be at a higher temperature with cryogenic plus natural ageing.
- The activation energy of the η' phase was found to be the highest in the CNA 10 specimen.
- After 40 days of natural ageing, texture changes were observed in all specimen.
- It has been calculated that the strain value is high in the planes with the dominant texture.
- With 100 days of natural ageing after cryogenics, the highest hardness value was obtained in the CNA100 sample as 175 HV 0.5. Overall, cryogenic plus natural ageing treatments increased hardness by approximately 15% in all specimens.
- The presence of white coloured secondary phases ($\text{Al}_{23}\text{CuFe}_4$ ve $\text{Al}_7\text{Cu}_2\text{Fe}$) was observed in the microstructures after cryogenic treatment. Based on the result of EDS analyses, these phases were composed of elements containing Cu and Fe.

Acknowledgements This study has been financially supported by the Gazi University Scientific Research Projects Coordination Unit [under Project Number FGA-2023-8195].

Funding This study was funded by Gazi Üniversitesi, FDK-2023-7620, Bülent Bostan.

Declarations

Conflict of interest The authors report no potential conflict of interest.

References

1. Hirsch J. Recent development in aluminium for automotive applications. *Trans Nonferrous Met Soc China*. 2014;24(7):1995–2002. [https://doi.org/10.1016/S1003-6326\(14\)63305-7](https://doi.org/10.1016/S1003-6326(14)63305-7).

2. Kodetová V, Vlach M, Kudrnová H, Leibner M, Málek J, Cieslar M, Neubert V. Annealing effects in commercial aluminium hot-rolled 7075 (–Sc–Zr) alloys. *J Therm Anal Calorim*. 2020;142(5):1613–23. <https://doi.org/10.1007/s10973-020-10249-1>.
3. Zhao H, Gault B, Ponge D, Raabe D. Reversion and re-aging of a peak aged Al–Zn–Mg–Cu alloy. *Ser Mater*. 2020;188:296–273. <https://doi.org/10.1016/j.scriptamat.2020.07.049>.
4. Omer K, Abolhasani A, Kim S, Nikdejad T, Butcher C, Wells M, Worswick M. Process parameters for hot stamping of AA7075 and D-7xxx to achieve high performance aged products. *J Mater Process Technol*. 2018;257:170–9. <https://doi.org/10.1016/j.jmatp.2018.02.039>.
5. Liu S, Li C, Han S, Deng Y, Zhang X. Effect of natural aging on quench-induced inhomogeneity of microstructure and hardness in high strength 7055 aluminum alloy. *J Alloy Compd*. 2015;625:34–43. <https://doi.org/10.1016/j.jallcom.2014.10.195>.
6. Erhard H. Hundred years of precipitation hardening. *J Light Met*. 2001;1(2):127–32. [https://doi.org/10.1016/S1471-5317\(01\)00006-2](https://doi.org/10.1016/S1471-5317(01)00006-2).
7. Leacock AG, Howe C, Brown D, Lademo OG, Deering A. Evolution of mechanical properties in a 7075 Al-alloy subject to natural ageing. *Mater Des*. 2013;49:160–7. <https://doi.org/10.1016/j.matdes.2013.02.023>.
8. Ayer R, Koo JY, Steeds JW, Park BK. Microanalytical study of the heterogeneous phases in commercial Al–Zn–Mg–Cu alloys. *Metall Trans A*. 1985;16(11):1925–36. <https://doi.org/10.1007/BF02662393>.
9. Deschamps A, Bley F, Livet F, Fabregue D, David L. In-situ small-angle X-ray scattering study of dynamic precipitation in an Al–Zn–Mg–Cu alloy. *Philos Mag*. 2003;83(6):677–92. <https://doi.org/10.1080/0141861021000051091>.
10. Dehghani K, Nekahi A, Mirzaie MAM. Optimizing the bake hardening behavior of Al7075 using response surface methodology. *Mater Des*. 2010;31(4):1768–75. <https://doi.org/10.1016/j.matdes.2009.11.014>.
11. Dlubek G, Krause R, Brümmer O, Plazaola F. Study of formation and reversion of Guinier-Preston zones in Al-4.5 at % Zn-x at % Mg alloys by positrons. *J Mater Sci*. 1986;21(3):853–858. <https://doi.org/10.1007/BF01117364>.
12. Berg LK, Gjønnes J, Hansen VX, Li XZ, Knutson-Wedel M, Schryvers D, Wallenberg LR. GP-zones in Al–Zn–Mg alloys and their role in artificial aging. *Acta Mater*. 2001;49(17):3443–51. [https://doi.org/10.1016/S1359-6454\(01\)00251-8](https://doi.org/10.1016/S1359-6454(01)00251-8).
13. Chung TF, Yang YL, Huang BM, Shi Z, Lin J, Ohmura T, Yang JR. Transmission electron microscopy investigation of separated nucleation and in-situ nucleation in AA7050 aluminium alloy. *Acta Mater*. 2018;149:377–87. <https://doi.org/10.1016/j.actamat.2018.02.045>.
14. Löffler H, Kovács I, Lendvai J. Decomposition processes in Al–Zn–Mg alloys. *J Mater Sci*. 1983;18(8):2215–40. <https://doi.org/10.1007/BF00541825>.
15. Hou S, Zhang D, Ding Q, Zhang J, Zhuang L. Solute clustering and precipitation of Al-5.1 Mg-0.15 Cu-xZn alloy. *Mater Sci Eng A*. 2019;759:465–478. <https://doi.org/10.1016/j.msea.2019.05.066>.
16. Ozer M, Dalli K, Ozer A. Effect of ball-burnishing on surface integrity and fatigue behaviour of 7175–T6 AA. *Mater Sci Technol*. 2023;39(2):248–57. <https://doi.org/10.1080/02670836.2022.2142744>.
17. Inoue H, Sato T, Kojima Y, Takahashi T. The temperature limit for GP zone formation in an Al–Zn–Mg alloy. *Metall Mater Trans A*. 1981;12(8):1429–34. <https://doi.org/10.1007/BF02643687>.
18. Chen J, Zhen L, Yang S, Shao W, Dai S. Investigation of precipitation behavior and related hardening in AA 7055 aluminum alloy. *Mater Sci Eng A*. 2009;500(1–2):34–42. <https://doi.org/10.1016/j.msea.2008.09.065>.

19. Lin YC, Jiang YQ, Zhang JL, Chen XM. Influence of stress-ageing processing on precipitates and mechanical properties of a 7075 aluminum alloy. *Adv Eng Mater*. 2018;20(1):1700583. <https://doi.org/10.1002/adem.201700583>.
20. Xu X, Zheng J, Li Z, Luo R, Chen B. Precipitation in an Al-Zn-Mg-Cu alloy during isothermal aging: atomic-scale HAADF-STEM investigation. *Mater Sci Eng A*. 2017;691:60–70. <https://doi.org/10.1016/j.msea.2017.03.032>.
21. Hansen V, Karlsen OB, Langsrud Y, Gjønnes J. Precipitation and strengthening in aluminium alloys. *Mater Sci Technol*. 2004;20(2):185–93. <https://doi.org/10.1179/026708304225010424>.
22. Lendvai J. Precipitation and strengthening in aluminium alloys. *Mater Sci Forum*. 1996;217:43–56. <https://doi.org/10.4028/www.scientific.net/MSF.217-222.43>.
23. Sha G, Cerezo A. Early-stage precipitation in Al–Zn–Mg–Cu alloy (7050). *Acta Mater*. 2004;52(15):4503–16. <https://doi.org/10.1016/j.actamat.2004.06.025>.
24. Liu J, Hu R, Zheng J, Zhang Y, Ding Z, Liu W, Sha G. Formation of solute nanostructures in an Al–Zn–Mg alloy during long-term natural aging. *J Alloy Compd*. 2020;821:153572. <https://doi.org/10.1016/j.jallcom.2019.153572>.
25. Chatterjee A, Qi L, Misra A. In situ transmission electron microscopy investigation of nucleation of GP zones under natural aging in Al–Zn–Mg alloy. *Scr Mater*. 2022;207:114319. <https://doi.org/10.1016/j.scriptamat.2021.114319>.
26. Khalfallah A, Raho AA, Amzert S, Djemli A. Precipitation kinetics of GP zones, metastable η' phase and equilibrium η phase in Al–5.46 wt.% Zn–1.67 wt.% Mg alloy. *Trans Nonferrous Met Soc China*. 2019;29(2):233–241. [https://doi.org/10.1016/S1003-6326\(19\)64932-0](https://doi.org/10.1016/S1003-6326(19)64932-0).
27. Schneider R, Heine B, Grant RJ, Zouaoui Z. Mechanical behaviour of aircraft relevant aluminium wrought alloys at low temperatures. *Proc Inst Mech Eng Part L J Mater Des Appl*. 2015;229(2):126–36. <https://doi.org/10.1177/1464420713501734>.
28. Yuan S, Cheng W, Liu W, Xu Y. A novel deep drawing process for aluminum alloy sheets at cryogenic temperatures. *J Mater Process Technol*. 2020;284:116743. <https://doi.org/10.1016/j.jmatprotec.2020.116743>.
29. Yin X, Deng W, Zou Y, Zhang J. Ultrafine grained Al 7075 alloy fabricated by cryogenic temperature large strain extrusion machining combined with aging treatment. *Mater Sci Eng A*. 2019;762:138106. <https://doi.org/10.1016/j.msea.2019.138106>.
30. Kissinger HE. Reaction kinetics in differential thermal analysis. *Anal Chem*. 1957;29(11):1702–6.
31. Takhor RL. Advances in nucleation and crystallization of glasses. *Am Ceram Soc Columb*. 1971;166:10–2.
32. Augis JA, Bennett JE. Calculation of the avrami parameters for heterogeneous solid state reactions using a modification of the kissinger method. *J Therm Anal*. 1978;13(2):283–92. <https://doi.org/10.1007/BF01912301>.
33. Hulett JR. Deviations from the arrhenius equation. *Q Rev Chem Soc*. 1964;18(3):227–42. <https://doi.org/10.1039/QR9641800227>.
34. Taskesen A, Aksoz S, Ozdemir A. The effect of cryogenic treatment on ageing behaviour of B4C reinforced 7075 aluminium composite. *Kovove Mater-Met Mater*. 2017;55(1):57–67. https://doi.org/10.4149/km_2017_1_57.
35. Davis JR. Aluminum and aluminum alloys. ASM International. 1993;3:534–642.
36. Warren BE. X-ray diffraction. Courier Corporation. 1990;1:7–10.
37. Harris GBX. Quantitative measurement of preferred orientation in rolled uranium bars. *The Lond Edinb Dublin Philos Mag J Sci*. 1952;43(336):113–23. <https://doi.org/10.1080/14786440108520972>.
38. Smallman RE. Modern physical metallurgy. 2016;4:385–491.
39. Holzwarth U, Gibson N. The Scherrer equation versus the 'Debye-Scherrer equation. *Nat Nanotechnol*. 2011;6(9):534–534. <https://doi.org/10.1038/nnano.2011.145>.
40. Williamson GK, Hall WH. X-ray line broadening from filed aluminium and wolfram. *Acta Metall*. 1953;1(1):22–31. [https://doi.org/10.1016/0001-6160\(53\)90006-6](https://doi.org/10.1016/0001-6160(53)90006-6).
41. Hansen N. Hall-Petch relation and boundary strengthening. *Scr Mater*. 2004;51(8):801–6. <https://doi.org/10.1016/j.scriptamat.2004.06.002>.
42. Martin JW. Micromechanisms in particle-hardened alloys. Cambridge: Cambridge University; 1980.
43. Ozawa T. Kinetic analysis of derivative curves in thermal analysis. *J Therm Anal*. 1970;2(3):301–24. <https://doi.org/10.1007/BF01911411>.
44. Papazian JM. Calorimetric studies of precipitation and dissolution kinetics in aluminum alloys 2219 and 7075. *Metall Trans A*. 1982;13(5):761–9. <https://doi.org/10.1007/BF02642389>.
45. Fanfoni M, Tomellini M. The johnson-mehl-avrami-kohnogorov model: a brief review. *Il Nuovo Cimento D*. 1998;20(7):1171–82. <https://doi.org/10.1007/BF03185527>.
46. Callister JR, William D, David G. Rethwisch. Fundamentals of materials science and engineering an integrated approach. 2020;261–79.
47. Altuntaş G, Altuntaş O, Bostan B. Characterization of Al-7075/T651 alloy by RRA heat treatment and different pre-deformation effects. *Trans Indian Inst Met*. 2021;74(12):3025–33. <https://doi.org/10.1007/s12666-021-02369-5>.
48. Altuntaş G, Bostan B. Metallurgical characterization of natural aging effects on pre-deformed Al 7075/T651 alloy during retrogression and re-aging heat treatment. *Kovove Mater-Met Mater*. 2022;60(4):209–222. <https://doi.org/10.31577/km.2022.4.209>.
49. Guo W, Guo J, Wang J, Yang M, Li H, Wen X, Zhang. Evolution of precipitate microstructure during stress aging of an Al–Zn–Mg–Cu alloy. *J Mater Sci Eng A*. 2015;634:167–175. <https://doi.org/10.1016/j.msea.2015.03.047>.
50. Gao M, Feng CR, Wei RP. An analytical electron microscopy study of constituent particles in commercial 7075–T6 and 2024–T3 alloys. *Metall Mater Trans A*. 1998;29(4):1145–51. <https://doi.org/10.1007/s11661-998-0240-9>.

Publisher's Note Springer Nature remains neutral with regard to jurisdictional claims in published maps and institutional affiliations.

Springer Nature or its licensor (e.g. a society or other partner) holds exclusive rights to this article under a publishing agreement with the author(s) or other rightsholder(s); author self-archiving of the accepted manuscript version of this article is solely governed by the terms of such publishing agreement and applicable law.